In Situ Direct Method To Massively Prepare Hydrophilic Porous Carbide-Derived Carbons for High-Performance Supercapacitors

Hai Su,[†,∥] Haichao Huang,[†,∥] Haitao Zhang,*[†] Xiang Chu,[†] Binbin Zhang,[†] Bingni Gu,[†] Xiaotong Zheng,[†] Songhao Wu,[§] Weidong He,[§] Cheng Yan,[†] Jun Chen,*[‡] and Weiqing Yang*[†]

[†]Key Laboratory of Advanced Technologies of Materials (Ministry of Education), School of Materials Science and Engineering, Southwest Jiaotong University, Chengdu, Sichuan 610031, China

[‡]Department of Materials Science and Engineering, Stanford University, Stanford, California 94305, United States

[§]School of Physics, University of Electronic Science and Technology of China, Chengdu, Sichuan 611731, China

S *Supporting Information*

ABSTRACT: To build a high-performance supercapacitor, chemical surface modification and hierarchically porous construction are two widely adopted routes for electrode materials design. Unfortunately, they are suffering from perplexing steps and low yield. Herein, we reported an in situ direct method to massively prepare hierarchically porous carbide-derived carbons with nitrogen and chlorine co-doping (CDCs-N/Cl) via etching $TiC_{0.5}N_{0.5}$ in chlorine-containing atmosphere. The as-prepared CDCs-N/Cl with high ratio of heteroatoms exhibited superhydrophilicity and delivered a maximum specific capacitance of 277.7 F g^{-1} in 6 M KOH,

which is the highest value among all the reported CDC materials. Besides, the assembled asymmetrical supercapacitor shows remarkable specific capacitance of 233.4 F g^{-1}, and 97% initial capacitance can be retained after 20,000 cycles at 2 A g^{-1}, revealing excellent cycling stability. This work is expected to pave a new way for rapid and scalable supercapacitive electrode materials production.

KEYWORDS: *hierarchical pores, heteroatoms doping, carbide-derived carbons, supercapacitors, superhydrophilicity, electrochemical performance*
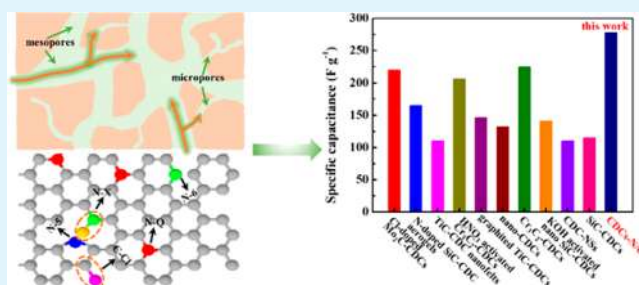
INTRODUCTION

Featured with high power capability, fast charge/discharge rate, and remarkable cyclability, supercapacitors are widely employed as power sources in modern electric vehicles, portable electronics, and many others.[1−5] Hierarchically porous carbons with high specific surface area (SSA) are popular electrode materials for supercapacitors owing to their tunable pore size, high electrochemical stability, and decent conductivity, which can facilitate both electron transportation and ion permeability to enhance both energy and power density.[6−9] To design the desired carbon electrode for supercapacitors, both material inner hierarchical porous structure and surface wettability are very critical factors. On one hand, a proper pore size can not only promote ion desolvation[10,11] but also provide fast ions transport pathways with a minimized resistance for ion moving.[12−14] On the other hand, to improve the electrode wettability, introducing hydrophilic functional groups (carbonyl, epoxy, and so on) and doping with heteroatoms (such as N, S, P, and Cl, etc.) are two widely reconginzed techniques. For instance, N doping can not only improve the electrical conductivity, increase the charge screening ability of carbon, but also facilitate charge transfer across the electrode/electrolyte interface, introducing

pseudocapacitance to enhance the capacitance of super-capacitors.[15−24]

Carbide-derived carbons (CDCs) have stood out recently in all the porous carbon materials by delivering ultrahigh capacitance, originating from the accurate control of the pore size distribution (PSD) for the desolvated electrolyte ions.[25,26] As novel porous carbons, CDCs are commonly generated from selectively extracting metal or metalloid atoms from various carbides (including TiC, SiC, Mo_2C, Fe_3C, B_4C, and NbC, etc.) lattice layer by layer at an elevated temperature in a chlorine-containing atmosphere.[27−33] Among all these carbides, TiC with a small and uniform C−C bond length can result in narrowly distributed porous carbons, which makes it a promising precursor to produce CDCs.[34] Gogotsi et al. have demonstrated that the TiC-CDC electrodes can deliver ultrahigh capacitance, originating from both the accurate control of the PSD and matching pore diameter with the size of the desolvated electrolyte ions.[10] However, the capacitance decreases quickly with increasing voltage scan rate or current
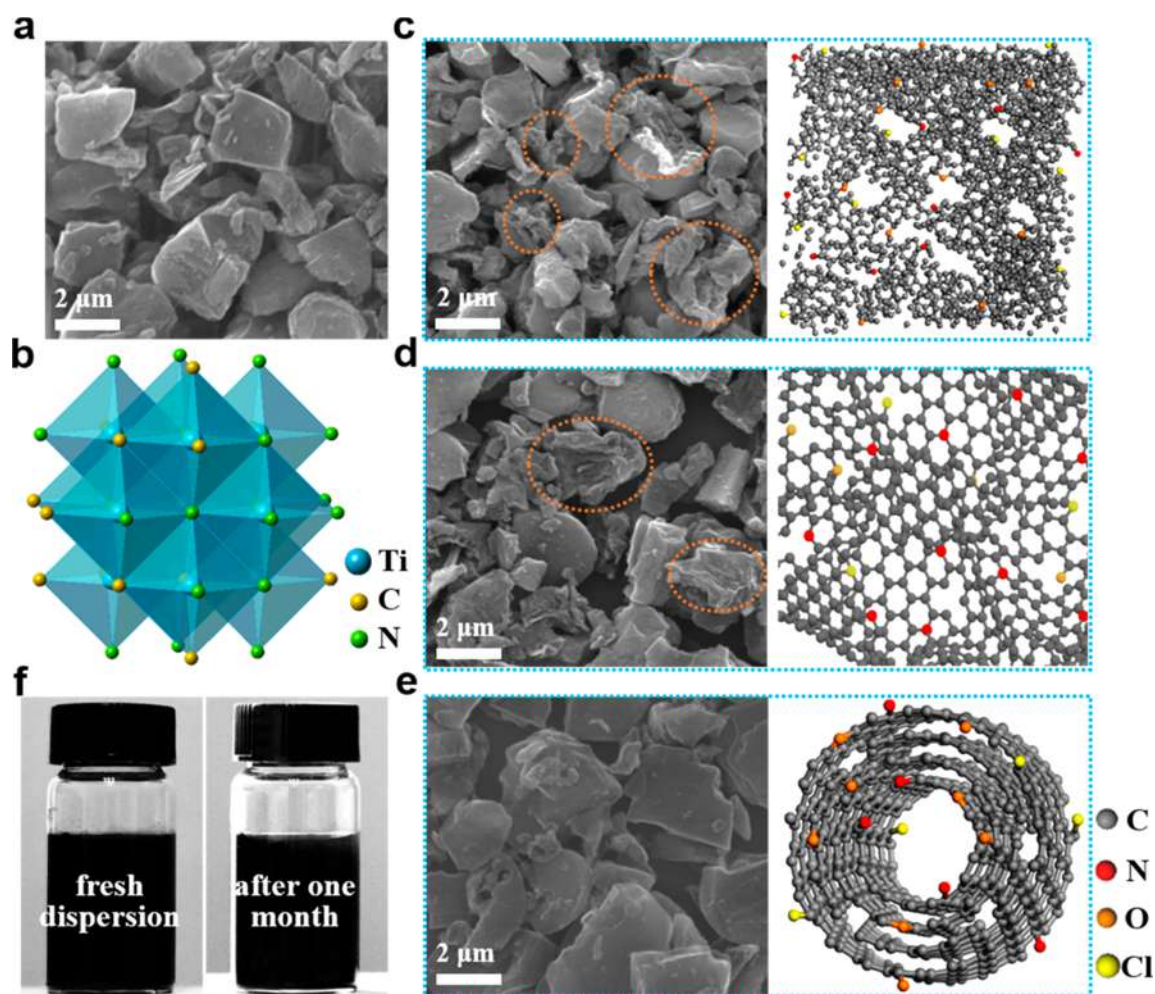
Figure 1. (a) A SEM image of the used $TiC_{0.5}N_{0.5}$ powders. (b) Cubic crystal structure of $TiC_{0.5}N_{0.5}$. SEM image and its microstructure schematic diagram of (c) CDC-N/Cl-700, (d) CDC-N/Cl-800, and (e) CDC-N/Cl-1000. Dashed circles indicated the corrugated domains. (f) Photography of CDC-N/Cl-800 powders dispersed in deionized water at a concentration of 1.5 mg mL^{-1} and the bottle of mixture staying still after 1 month.

density because the electrolytes cannot swimmingly transport in small pores of carbon electrodes.[35] However, hierarchical porous structure with mesoporous channel pores and the micropores drilled on the mesopore walls are beneficial to maintain high capacitance and simultaneously achieve excellent rate capability.[36]

In this regard, CDCs is a promising candidate as desired electrode materials for high-performance supercapacitors, but they still suffer from the perplexing synthesis steps and low yield largely, hindering their further advancement for practical usage. Herein, we present an in situ direct method to massively prepare hierarchically porous carbide-derived carbons with nitrogen and chlorine co-doping (CDCs-N/Cl) via etching ($TiC_{0.5}N_{0.5}$) in chlorine-containing atmosphere. With increasing chlorination temperatures, the microstructure gradually transformed from amorphous carbons to ordered graphite ribbons and carbon onions. And the contents of N and Cl atoms were decreased due to the thermal decomposition of carbon nitrides and the removal of remnant chlorines. With optimized electrode wettability, heteroatoms-doped levels, and the porosity, the as-fabricated supercapacitors possess combining advantages of multi-heteroatoms doping for additional pseudocapacitance and hierarchically micro- to mesoporous channels for fast ion transport. As a consequence, the CDCs-N/Cl demonstrated a collection of compelling features,

including ultrahigh specific capacitance (277.7 F g^{-1}), good rate capability, and excellent capacitance retention (97% retainability after 20,000 cycles at 2 A g^{-1}). In a word, this work reported an efficient method to rapidly and massively produce electrode materials. It is expected to pave a practical way for electrode materials design toward high-performance energy storage systems.

■ RESULTS AND DISCUSSION

To synthesize CDCs-N/Cl, the rock-salt structure $TiC_{0.5}N_{0.5}$ powders were used as chlorination precursor, as the scanning electron microscopy (SEM) image and sketch respectively shown in Figure 1a,b. Detailed experimental methods are presented in the Experimental Section (Supporting Information). Due to the strong oxidizing ability of Cl atoms, the Ti atoms were extracted from $TiC_{0.5}N_{0.5}$ via Ti−C and Ti−N bonds breakage, forming solid CN_xCl_y to obtain N and Cl co-doping, while releasing gaseous $TiCl_4$ and N_2 with the Ar flow. The fabrication process of the CDCs-N/Cl is straightforward and compatible with possible large-scale synthesis.

Via varying the chlorination temperatures, the blocked $TiC_{0.5}N_{0.5}$ was transformed into carbon lumps and/or corrugated sheets. At the chlorination temperature of 700 °C (CDC-N/Cl-700), amorphous structure was observed with large amount of corrugated lamella carbon, as seen in the SEM
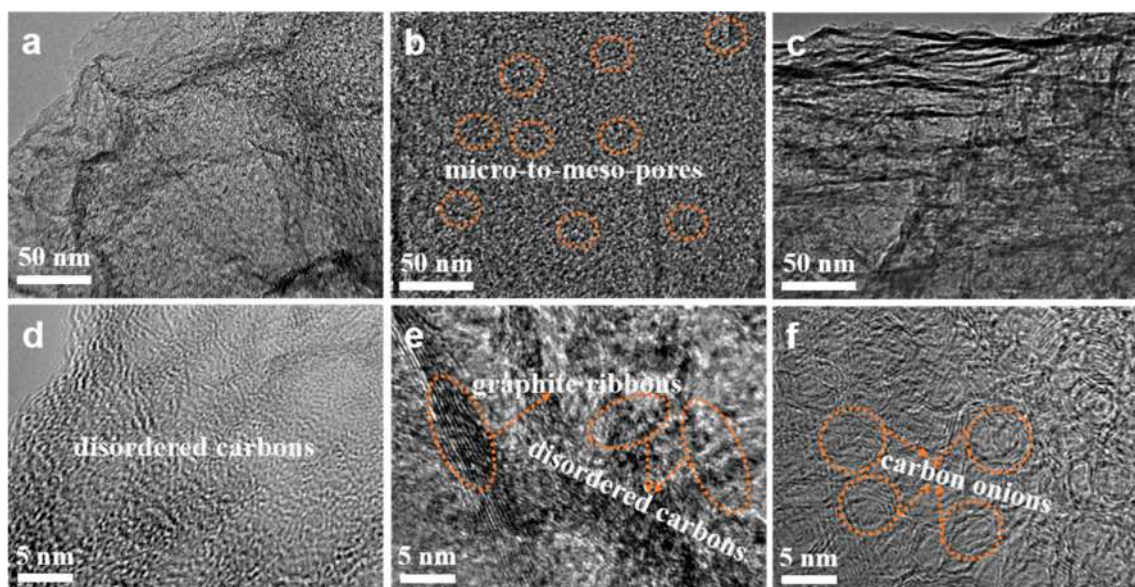
Figure 2. TEM images of the as-prepared (a) CDC-N/Cl-700, (b) CDC-N/Cl-800, and (c) CDC-N/Cl-1000. HRTEM images of the as-prepared (d) CDC-N/Cl-700, (e) CDC-N/Cl-800, and (f) CDC-N/Cl-1000, showing that the microstructures were transformed from amorphous to short-range ordered graphite (orange dashed ellipses) and further to onion-like crystalline (orange dashed circles).

image shown in Figure 1c. The transformation of block-shaped carbons into corrugated morphologies is mainly ascribed to the thermodynamics of carbides reaction with chlorine. At relatively low temperature, the undesired CCl_4 can be formed based on the reaction equation of $C(s) + 2Cl_2(g) \rightarrow CCl_4(g)$, which has broken down the carbon framework and resulted in shrinking in different directions to form corrugated lamella carbon,[37] while in the temperature range from 800 °C (CDC-N/Cl-800) to 900 °C (CDC-N/Cl-900), the corrugated lamella carbon gradually decreases with the shorter complete chlorination time of CDC-N/Cl-800 (Figures 1d and S1). At chlorination temperature of 1000 °C (CDC-N/Cl-1000), it shows a single block-shape morphology due to the shorter reaction time and turns into an onion-like crystalline shape (Figure 1e). The introduction of N and Cl heteroatoms into the carbon lattice will not only design the hierarchically porous structure but also improve the hydrophilicity of the carbon material. The obtained CDCs-N/Cl were mixed with deionized water at a concentration of 1.5 mg mL^{-1}, and no precipitation was observed even when the dispersion stayed still for 1 month (Figures 1f and S2).

To further investigate the chlorination temperature dependent morphology variation of CDCs-N/Cl, transmission electron microscopy (TEM) and high-resolution transmission electron microscopy (HRTEM) were employed (Figures 2 and S3). A large number of pores were presented on the carbon surface owing to the Cl/Ti atoms reaction in the lattice framework and releasing of gaseous TiCl$_4$. All the CDCs-N/Cl samples presented abundant of micro- to mesopores. Both the pores' size and density were first increased with the elevation of chlorination temperatures, and maximized at 800 °C. With further increasing of the temperature, partial pores started to disappear (Figures 2a–c and S3a). HRTEM was also utilized to verify the temperature resulted structural differences. Almost disordered carbons were observed for CDC-N/Cl-700 (Figure 2d). While partially ordered graphite lattice accompanying with predominant disordered amorphous carbon were found in both CDC-N/Cl-800 (Figure 2e) and CDC-N/Cl-900 (Figure

S3b), as highlighted with orange dashed ellipses. For CDC-N/Cl-1000, as shown in Figure 2f, the amorphous structure transformed into ordered crystalline grain-like carbon onions, as pointed out with orange dashed circles.

In addition, the CDCs-N/Cl microstructure evolution was also justified via X-ray Diffraction (XRD) . As shown in Figure S4a, TiC$_{0.5}$N$_{0.5}$ powders presented five characteristic peaks between 10° and 80°. With the optimized reaction time, TiC$_{0.5}$N$_{0.5}$ can be completely transformed into CDCs with two broad diffraction peaks at 2θ around 26° and 43° under different temperatures, which were respectively assigned to the (002) and (101) crystallographic planes of the carbon materials (Figure S4b). It is worth noting that the chlorination degree depends on both chlorination temperature and reaction time, which takes shorter reaction time to realize the same transformation at higher chlorination temperature (Figure S5). Typically, with the sample chlorination at 800 °C for 3 h, residual precursor diffraction peaks can be observed. While an increase of the reactive time to 4 h can obtain perfect CDC-N/Cl-800.

Proper porosity is very critical for the CDCs-N/Cl to abtain decent electrochemical performance. As demonstrated in Figure 3a, the isotherms of all of the CDCs-N/Cl exhibit the typical types I and IV hysteresis loops, proving the existence of micropores and mesopores.[38–40] The multipoint BET results evidentially justified the strong influences of chlorination temperature on the sample SSA value. It was firstly increased with the elevated chlorination temperatures and reached the maximum value of 1453.8 m^2 g^{-1} at 800 °C. With a further increasing of the chlorination temperature beyond 900 °C, the SSA value is decreased to 695.8 m^2 g^{-1}. The pore size distribution (PSD) curves, obtained by using the density functional theory (DFT) method, exhibit three noticeable peaks centered at ~0.7, 1.7, and 3.4 nm, evidently demonstrating the hierarchical porous structure from micropores (<2 nm) to mesopores (between 2 and 50 nm) of the CDCs-N/Cl (Figure 3b). The unique hierarchical porous structure in the CDCs-N/Cl is beneficial to the electrolyte
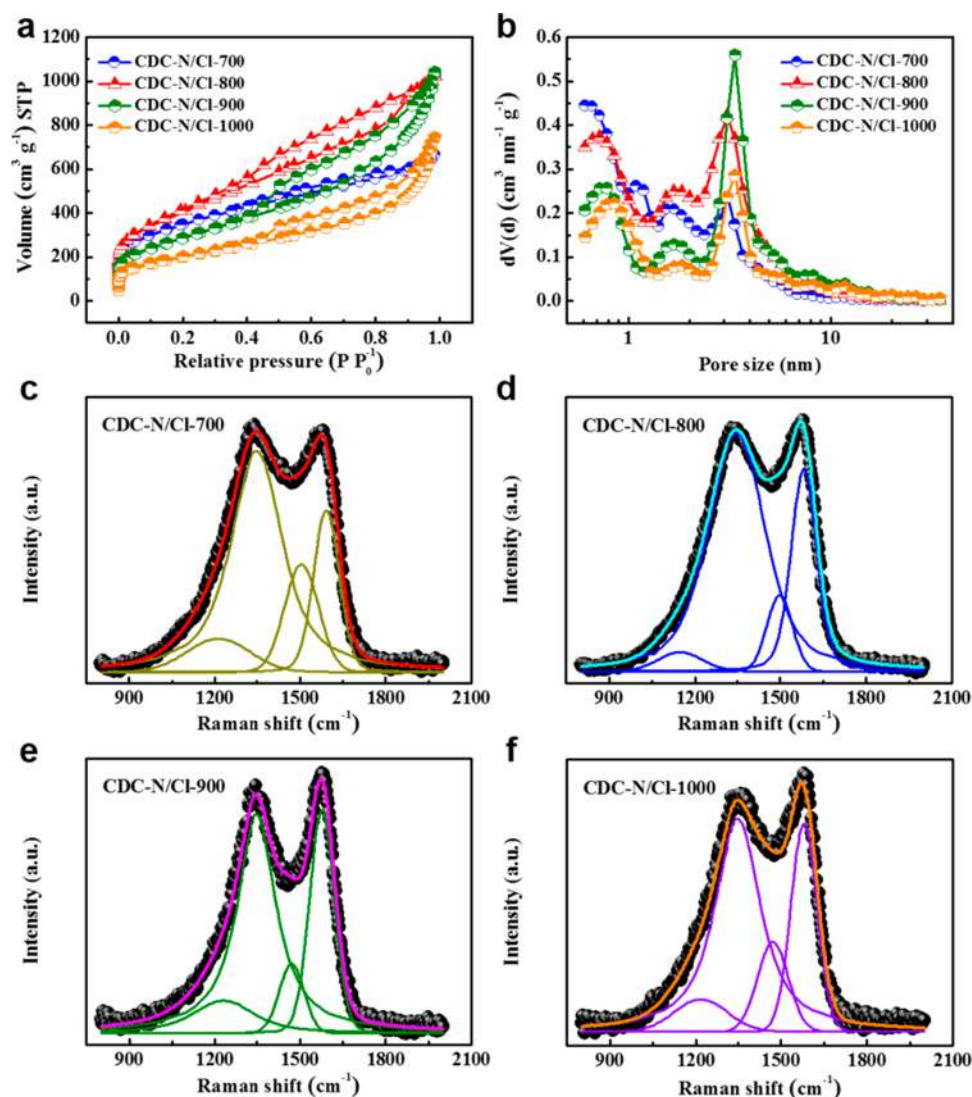
Figure 3. (a) N_2 absorption/desorption isotherms. (b) Corresponding pore size distribution curves obtained by using DFT method. Raman spectra of the as-prepared (c) CDC-N/Cl-700, (d) CDC-N/Cl-800, (e) CDC-N/Cl-900, and (f) CDC-N/Cl-1000. Four Vigot functions were used to fit the results.

accommodation and ions transport. Moreover, the corresponding total pore volume showed a change tendency similar to that of SSA with elevation of chlorination temperatures, as displayed in Table S2. It is attributed to the partially structural collapse of pore walls due to the selective replacement of Ti atoms by C and N atoms. These observations are also verified by the HRTEM.

For a systematical characterization, Raman spectra was also applied to study the evolution of microstructure and structural defects of CDCs-N/Cl, as the results shown in Figure 3c−f. Two noticeable characteristic peaks D and G band were respectively observed at 1350 and 1580 cm^{-1}. The former peak was originated from the breathing mode with A_{1g} symmetry, and the latter one was due to the graphite in-plane bond-stretching motion of the pairs of carbon atoms in sp^2 configuration with E_{2g} symmetry.[41−43] All of the samples demonstrated a broad and strong D band peak, obviously implying the presence of high-ratio disordered structure in CDCs-N/Cl. Moreover, the intensity of D band (I_D) was higher than that of G band (I_G) at 800 °C, while the D band became weaker as the chlorination temperature was raised

above 800 °C. Accordingly, a decreasing of the average I_D/I_G values from 3.05 ± 0.45 to 2.23 ± 0.05 when temperature increased from 700 to 1000 °C, clearly indicated that the carbons gradually became more ordered with increasing chlorination temperatures. The I_D/I_G values were determined by the multipeak fit of four Voigt functions for D′, D, D″, and G bands (Figure S6 and Table S3). The D′ and D″ bands represent transpolyacetylene-like chains at both layer edges and amorphous carbon and five-/seven-membered rings linking the aromatic regions, respectively.[44,45]

Besides the microstructure characterization, the chemical composition of CDCs-N/Cl were also studied by using X-ray photoelectron spectroscopy (XPS), as seen in the results shown in Figures 4 and S7. The XPS survey spectra (Figure 4a) confirmed the presence of C, N, and O in all the CDC-N/Cl samples, and a small amount of Cl can be detected due to the formation of C−Cl bond in the chlorination process. Besides, negligible Ti can also be observed, indicating the accomplishment of chlorine etching to the precursor. The detailed compositions calculated from the XPS survey spectra are shown in Table S4. For the Ti content, the highest value
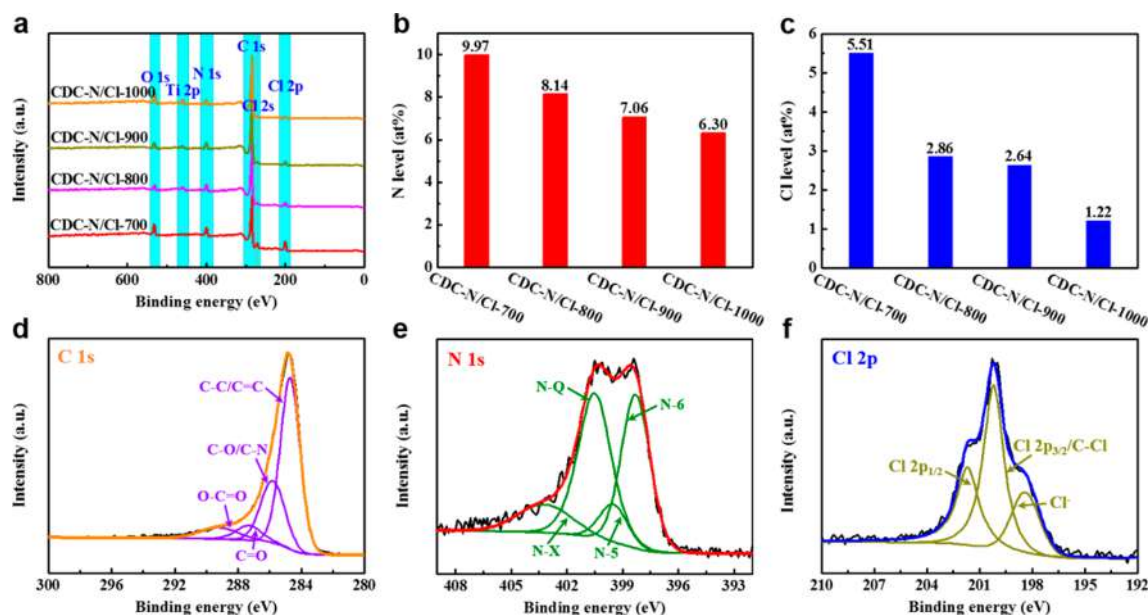
Figure 4. (a) XPS survey spectra. (b) N levels. (c) Cl levels. Deconvoluted high-resolution (d) C 1s, (e) N 1s, and (f) Cl 2p spectra of CDC-N/Cl-800.

(1.41 at%) is found in the CDC-N/Cl-1000 due to the relatively short reaction time. Moreover, the N and Cl amounts decreased with the increasing reaction temperature (Figure 4b,c), which is ascribed to the chlorination resulted N loss and carbon nitride decomposition.

In addition, energy-dispersive X-ray spectroscopy (EDS) was also employed to characterize the elemental distribution of CDC-N/Cl-800, as shown in Figure S8. The C species is dominating in the products with a weight percent of 77.6 wt %. The O and N species respectively possess a weight percent of 8.3 and 8.2 wt %. The trace of O species is mainly attributed to the oxidation during chlorination and H_2O absorption in the air atmosphere. Due to the Cl atoms doping, Cl species (3.9 wt %) was also detected. In addition, only very little Ti atoms (2.0 wt %) was detected, indicating that the vast majority of Ti species was extracted, which is consistent with the XPS results.

To obtain the detailed surface elemental information, the C 1s, N 1s, and Cl 2p high-resolution spectra of CDCs-N/Cl were deconvoluted. The high-resolution C 1s spectra can be fitted with four component peaks at 284.7, 285.8, 287.7, and 289.5 eV (Figures 4d and S7a−c). Among them, the peak located at 284.7 eV is ascribed to sp^2 carbon atoms bound to neighboring carbon atoms. While the peaks located at 285.8 and 287.7 eV can be respectively assigned to C−O and C=O, the peak located at 289.5 eV is due to the O−C=O bond.[46,47] Moreover, the high-resolution N 1s spectra is dominated by four different peaks at 398.3, 399.6, 401.0, and 403.5 eV (Figures 4e and S7d−f). The peak at 398.3 eV refers to the N bound to two carbon atoms, donating one p electron to the conjugation with the aromatic π-conjugated rings, namely, pyridinic N (N-6). The peak at 399.6 eV is commonly ascribed to the pyrrolic N (N-5), which possesses good electron-poor characteristics and higher charge mobility. The peak at 401.0 eV corresponds to graphitic-like N or quaternary N (N-Q), which is incorporated into the graphene layer and replaces a carbon atom within graphene frameworks. For the peak at 403.5 eV, it is attributed to the pyridinic oxidized N (N-X).[48−52] Evidently, the percentages of N-6 and N-5 decreased respectively from 37.1% and 18.6% to 13.8% and 7.3% while

the proportion of N-Q increased from 32.7% to 49.9%, with increasing chlorination temperatures. Lastly, the high-resolution Cl 2p spectra of CDCs-N/Cl were presented in Figures 4f and S7g−i, in which three peaks, located at 198.2, 200.6, and 202.2 eV, can be respectively deconvoluted corresponding to Cl^-, Cl $2p_{3/2}$ and/or C−Cl, and Cl $2p_{1/2}$ groups.[53,54] According to their peak intensities, the ratio of C−Cl content to Cl-containing group is decreasing as the elevation of reactive temperatures.

A systematical characterization of the CDCs-N/Cl well demonstrated their hierarchically porous structure, high N, Cl co-doping, high SSA, and thus the great potential of acting as superior electrode materials for high-performance super-capacitors. The electrochemical characterization of CDCs-N/Cl was performed first in 6 M KOH aqueous electrolyte in a three-electrode configuration. As shown in Figure 5a, all the CDCs-N/Cl based electrodes exhibit rectangular-like cyclic voltammetry (CV) curves at a scan rate of 50 mV s^{-1} with a potential window of 1 V, indicating the characteristic of electrical double layer (EDL) capacitance. CDC-N/Cl-800 possesses the largest enclosed area, namely, the highest specific capacitance, comparing with that of CDC-N/Cl-700, CDC-N/Cl-900, and CDC-N/Cl-1000. Furthermore, the triangle-like galvanostatic charge−discharge (GCD) curves of CDC-N/Cl based electrodes are obtained at a current density of 0.5 A g^{-1} and shown in Figure S9a (Supporting Information), which justified the good EDL behavior again. Among them, the CDC-N/Cl-800 holds the longest charge or discharge time, thus the highest specific capacitance. Figure 5b presents the specific capacitance as a function of current densities. At a current density of 0.5 A g^{-1}, CDC-N/Cl-800 possesses the highest specific capacitance of 277.7 F g^{-1}, while for CDC-N/Cl-700, CDC-N/Cl-900, and CDC-N/Cl-1000, the values respectively are 227.7, 182.3, and 43.9 F g^{-1}. As shown in Figure 5c, the presented specific capacitance value of 277.7 F g^{-1} is the highest among all of the CDC materials, including Cl doping of ordered mesoporous carbon with few-layered graphene walls,[46] N-doped SiC-CDC aerogels,[50] TiC-CDC nanofelts,[55] and so on.[56−62] Even at high current density of 30
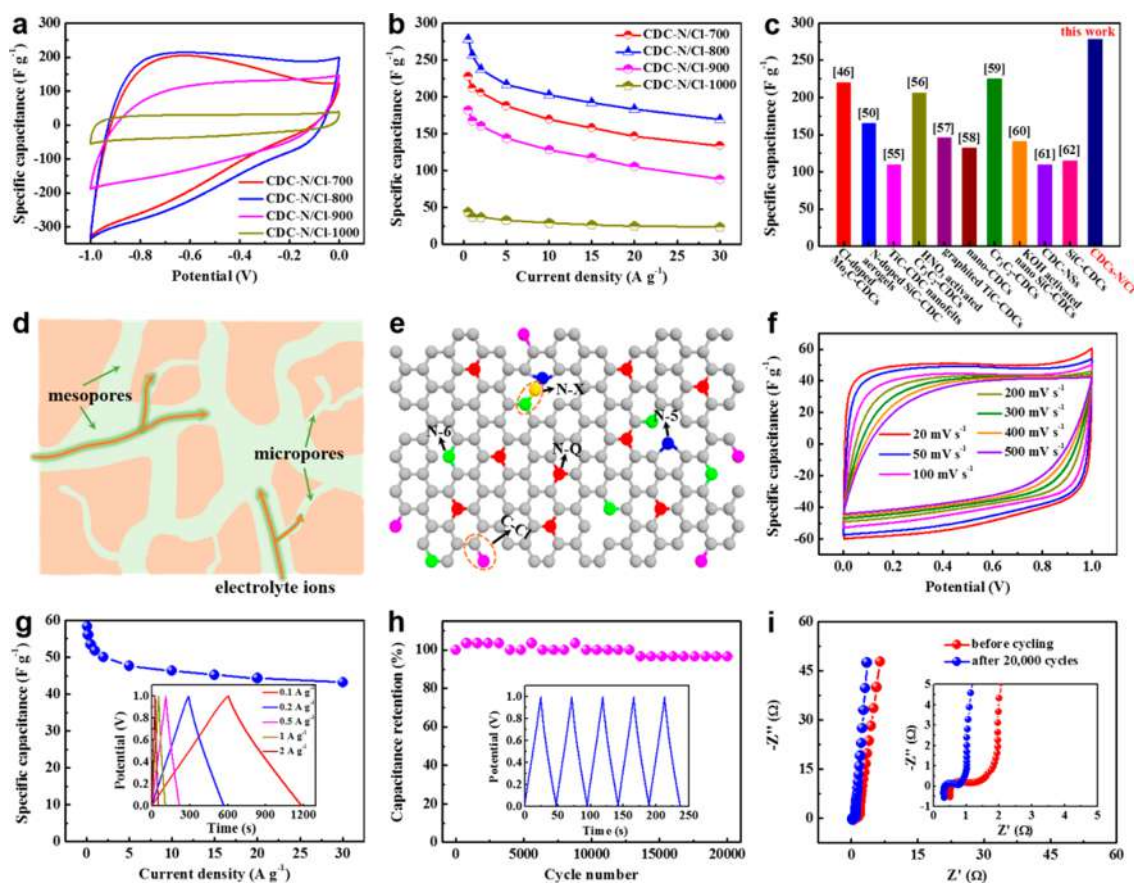
Figure 5. (a) CV curves of the various CDC-N/Cl electrodes at a scan rate of 50 mV s^{-1}. (b) Specific capacitance values versus current densities of the various CDC-N/Cl electrodes. (c) Specific capacitance comparison between CDC-N/Cl-800 and the other CDC materials in aqueous electrolyte. (d) Schematic hierarchically porous structure in the CDCs-N/Cl as electrode materials. The mesopores are conductive to the transportation of electrolyte ions, and numerous micropores support the accommodation of electrons, making a contribution to capacitance. (e) Sketch showing the possible locations for N and Cl atoms in a carbon network. (f) CV curves of the HPC6@CDC-N/Cl-800 asymmetrical supercapacitor at different scan rates between 20 and 500 mV s^{-1}. (g) Specific capacitance under diversified current densities. Inset represents the GCD curves at different current densities between 0.1 and 2 A g^{-1}. (h) Long-term cycling stability for 20,000 cycles at a current density of 2 A g^{-1}. Inset is the GCD curves for the last five cycles. (i) Nyquist plots before and after cycling stability measurement. Inset shows the high-frequency region.

A g^{-1}, the specific capacitance of CDC-N/Cl-800 can still maintain a value of 169.4 F g^{-1}.

Furthermore, under AC potential amplitude of 5 mV, the electrochemical AC impendence behaviors of CDCs-N/Cl are studied in the frequency ranges from 10^5 to 10^{-1} Hz, as shown in Figure S9b. The Nyquist plots exhibit the typical features of porous carbon with an arc at high frequencies, a 45° Warburg region at medium frequencies, and an almost vertical line at low frequencies. The most vertical line for CDC-N/Cl-800 electrode indicates the most capacitive characteristics at low frequencies. For CDC-N/Cl-800 electrode, an apparent 45° Warburg region at medium frequencies was observed, which is related to the diffusion of the ions into the electrode materials interface inside small pores. The equivalent series resistance (ESR) determined by the electrode materials, electrolyte, and the interface between electrode materials and current collector,[63,64] and the values are as low as 0.40−0.56 Ω for CDC-N/Cl electrodes. Moreover, we present the CV and GCD curves of CDC-N/Cl-800 electrode in Figure S9c,d, which further demonstrates the excellent electrochemical performance.

On one hand, the unique hierarchical porous architecture, dominated micropores and mesopores of CDC-N/Cl-800, favors rapid diffusion of electrolyte ions into the micropores located within the wall of mesopores, which could provide a fast diffusion channel through shortening the diffusion length (Figure 5d). On the other hand, an efficient interconnectivity of the porous channels can lead to much lower impedance for the transfer of the electrolyte ions through the channels and the micropores in the carbon wall, and thus showing better capacitive behavior and higher power density.[65,66] The good electrochemical properties of CDC-N/Cl-800 electrodes in return imply that most of the micropores within the mesoporous skeleton can be utilized effectively for charge storage. The micropores located at ∼0.7 nm contribute most to the formation of EDL capacitance, in consideration of the compatibility between the pore size and the desolvated K$^+$ ions with a diameter of 0.35−0.42 nm.[26] And mesopores centered at 3.4 nm efficiently promote the electrolyte ions diffusion and transfer for hierarchically porous CDC-N/Cl-800 samples.

Moreover, the hierarchical pores provide much more chemically active sites, such as electron-rich N and Cl atoms, to support a fast electrons and ions transfer path for forming pseudocapacitance in CDC-N/Cl-800 (Figure 5e). The electron-rich N and Cl doping increases the charge density and improves the polarity of the carbon matrix through the

interaction of free electrons with large π electrons in the carbon skeleton and thus high capacitance and power characteristics for CDC-N/Cl-800 electrodes. Finally, the effect of hierarchical pores can enhance the ion-accessible SSA, which in turn supplies much more effective chemically active sites to favor the formation of pseudocapacitance.[67] Thus, heteroatoms doping and hierarchically porous structure show a synergistic effect on electrochemical properties at low charge−discharge rates, while the latter contributes to high charge−discharge rates, demonstrating that outstanding electric conductivity of the doped carbon materials could guarantee both high energy and power density.

Two-electrode configuration evaluation is much more efficient. However, N, Cl co-doped CDCs with hierarchical pores are ideal negative electrode materials while only a specific capacitance of 41.9 F g^{-1} (167.6 F g^{-1} for a single electrode) was exhibited at a current density of 0.2 A g^{-1} because of their extremely low specific capacitance at positive voltage range (Figure S10). Hence, CDC-N/Cl-800 was employed as the negative electrode material to build up an asymmetrical supercapacitor, and hierarchically porous carbons (HPC6) were chosen as positive electrode because of their excellent capacitive performance (Figure S11). In Figure 5f, the CV curves exhibit perfect rectangular shapes from 0 to 1 V in a wide scanning range of 20−500 mV s^{-1}, indicating an excellent capacitive behavior and rate capability. And the shape becomes gradually distorted after scan rates beyond 500 mV s^{-1}, owing to the limited electrolyte ions diffusion kinetics. The GCD curves at different current densities ranging from 0.1 to 30 A g^{-1} are shown in the inset of Figures 5g and S12. All the curves resemble isosceles triangular shapes, indicating an ideal EDL behavior, even when the current density reaches up to 30 A g^{-1}. A minor drop of 0.28 V was observed at a high current density of 30 A g^{-1}, implying an internal resistance of 0.74 Ω, according to IR drop = $\Delta V/2I$. Besides, Figure 5g shows the specific capacitance values as a function of current densities, which are derived from the GCD curves. The HPC6@CDC-N/Cl-800 asymmetrical supercapacitor exhibits the highest specific capacitance of 58.3 F g^{-1} (233.4 F g^{-1} for a single electrode) at a current density of 0.1 A g^{-1} and then decreases to 43.2 F g^{-1} at 30 A g^{-1}, maintaining 74.1% of the initial capacitance.

In addition, the capacitance retention ability of supercapacitors at a fixed current density is a critical parameter. The long-term cycling test was conducted at a current density of 2 A g^{-1}. After 20,000 cycles, 97% of its initial capacitance can be retained (Figure 5h). Moreover, the inset (GCD curves) show a highly symmetrical isosceles triangle shape with insignificant changes in the last five cycles, demonstrating the excellent cycling stability. EIS analysis was conducted in the frequency range from 10^5 to 10^{-2} Hz at voltage of 5 mV (Figure 5i). The ohmic resistance is 0.54 Ω in the high-frequency region and shows no apparent change after cycling 20,000 cycles at 2 A g^{-1}, again indicating outstanding electrochemical stability. The interfacial charge transfer resistances (R_{ct}) located at the high-to-medium-frequency region are very low at 0.56 and 0.45 Ω before and after cycling, respectively. Moreover, Warburg impedance, a typical 45° phase angle in the medium-frequency region, decreases with cycling numbers, which is due to the improved ion diffusion. In addition, the nearly vertical line in the low-frequency region reveals the ideal capacitive behavior with good propagation characteristic of electrolyte ions at the electrode/electrolyte interface.[68,69]

These results ensure that HPC6@CDC-N/Cl-800 asymmetrical supercapacitor delivers a high energy of 8.1 Wh kg^{-1} at a power density of 0.05 kW kg^{-1} and then remains 6.0 Wh kg^{-1} at an exceedingly high power density of 15 kW kg^{-1} (Figure S13). In a word, the as-prepared CDC-N/Cl-800 electrode materials exhibit a collection of compelling features, including high specific capacitance, high rate capability, and excellent cyclic stability in comparison with previously reported CDCs based supercapacitors, as summarized in Table S5.

CONCLUSION

In conclusion, we prepared CDCs-N/Cl at large scale with superior electrochemical performance for supercapacitors using a rapid in situ direct etching method. By simply adjusting chlorination temperature and reaction time, the CDCs could be doped with a tunable amount of N (6.30−9.97 at. %) and Cl (1.22−5.51 at. %), and controllable pore size distribution (from micro- to mesoporous range) as well as high surface area up to 1453.8 m^2 g^{-1}. The CDC-N/Cl-800 electrode exhibited the highest specific capacitance of 277.7 F g^{-1} among all reported CDC materials so far in a three-electrode configuration, and a value of 233.4 F g^{-1} at 0.1 A g^{-1} as the negative electrode for asymmetrical supercapacitors. In the meanwhile, outstanding capacitance retention of 74.1% at a high current density of 30 A g^{-1} was achieved for the as-built asymmetrical supercapacitors. And after 20,000 cycles, 97% initial capacitance can be retained, indicating excellent cycling stability. The combination of multi-heteroatom doping and hierarchical pore design for CDCs overcame the present limitations of slow faradaic reaction and poor ion transport in traditional microstructured carbon . It is a practical advancement in supercapacitive electrode materials preparation toward high-performance supercapacitors.

ASSOCIATED CONTENT

⑤ Supporting Information

The Supporting Information is available free of charge on the ACS Publications website at DOI: 10.1021/acsaem.8b00764.

> Synthesis of CDCs-N/Cl and HPC6, materials characterization details, supercapacitor fabrication, additional microstructure morphologies, photographic images of the dispersion, detailed temperatures and times, XRD patterns, textural properties, Raman spectra, surface elemental analysis, EDS mapping analysis, electrochemical performance (PDF)

AUTHOR INFORMATION

Corresponding Authors

*E-mail: haitaozhang@swjtu.edu.cn (H.Z.).
*E-mail: chenjun@stanford.edu; junchenwelcome@gmail.com (J.C.).
*E-mail: wqyang@swjtu.edu.cn (W.Y.).

ORCID ⓘ

Xiaotong Zheng: 0000-0003-0489-3339
Weidong He: 0000-0001-8242-2888
Jun Chen: 0000-0002-3439-0495
Weiqing Yang: 0000-0001-8828-9862

Author Contributions

‖H.S. and H.H. contributed equally to this work. W.Y., J.C., and H.Z. supervised the whole project.

■ **REFERENCES**

(1) Simon, P.; Gogotsi, Y.; Dunn, B. Where Do Batteries End and Supercapacitors Begin? *Science* **2014**, *343*, 1210−1211.

(2) Wang, Y.; Song, Y.; Xia, Y. Electrochemical Capacitors: Mechanism, Materials, Systems, Characterization and Applications. *Chem. Soc. Rev.* **2016**, *45*, 5925−5950.

(3) Sheberla, D.; Bachman, J. C.; Elias, J. S.; Sun, C.-J.; Shao-Horn, Y.; Dincă, M. Conductive MOF Electrodes for Stable Supercapacitors with High Areal Capacitance. *Nat. Mater.* **2017**, *16*, 220−224.

(4) Liu, W.; Song, M.-S.; Kong, B.; Cui, Y. Flexible and Stretchable Energy Storage: Recent Advances and Future Perspectives. *Adv. Mater.* **2017**, *29*, 1603436.

(5) Li, S.; Yu, C.; Yang, J.; Zhao, C.; Zhang, M.; Huang, H.; Liu, Z.; Guo, W.; Qiu, J. A Superhydrophilic "Nanoglue" for Stabilizing Metal Hydroxides onto Carbon Materials for High-Energy and Ultralong-Life Asymmetric Supercapacitors. *Energy Environ. Sci.* **2017**, *10*, 1958−1965.

(6) Kim, T.; Jung, G.; Yoo, S.; Suh, K. S.; Ruoff, R. S. Activated Graphene-Based Carbons as Supercapacitor Electrodes with Macro- and Mesopores. *ACS Nano* **2013**, *7*, 6899−6905.

(7) Wu, S.; Chen, G.; Kim, N. Y.; Ni, K.; Zeng, W.; Zhao, Y.; Tao, Z.; Ji, H.; Lee, Z.; Zhu, Y. Creating Pores on Graphene Platelets by Low-Temperature KOH Activation for Enhanced Electrochemical Performance. *Small* **2016**, *12*, 2376−2384.

(8) Zhang, L. L.; Zhao, X.; Stoller, M. D.; Zhu, Y.; Ji, H.; Murali, S.; Wu, Y.; Perales, S.; Clevenger, B.; Ruoff, R. S. Highly Conductive and Porous Activated Reduced Graphene Oxide Films for High-Power Supercapacitors. *Nano Lett.* **2012**, *12*, 1806−1812.

(9) Xu, Y.; Lin, Z.; Zhong, X.; Huang, X.; Weiss, N. O.; Huang, Y.; Duan, X. Holey Graphene Frameworks for Highly Efficient Capacitive Energy Storage. *Nat. Commun.* **2014**, *5*, 4554.

(10) Chmiola, J.; Yushin, G.; Gogotsi, Y.; Portet, C.; Simon, P.; Taberna, P. L. Anomalous Increase in Carbon Capacitance at Pore Sizes Less Than 1 Nanometer. *Science* **2006**, *313*, 1760−1763.

(11) Chmiola, J.; Largeot, C.; Taberna, P.-L.; Simon, P.; Gogotsi, Y. Desolvation of Ions in Subnanometer Pores and Its Effect on Capacitance and Double-Layer Theory. *Angew. Chem., Int. Ed.* **2008**, *47*, 3392−3395.

(12) Lee, K.; Yoon, Y.; Cho, Y.; Lee, S. M.; Shin, Y.; Lee, H.; Lee, H. Tunable Sub-Nanopores of Graphene Flake Interlayers with Conductive Molecular Linkers for Supercapacitors. *ACS Nano* **2016**, *10*, 6799−6807.

(13) Zhang, H.; Zhang, X.; Ma, Y. Enhanced Capacitance Supercapacitor Electrodes from Porous Carbons with High Mesoporous Volume. *Electrochim. Acta* **2015**, *184*, 347−355.

(14) He, X.; Liu, Z.; Ma, H.; Zhang, N.; Yu, M.; Wu, M. Shell-Like Hierarchical Porous Carbons for High-Rate Performance Supercapacitors. *Microporous Mesoporous Mater.* **2016**, *236*, 134−140.

(15) Lin, T.; Chen, I.-W.; Liu, F.; Yang, C.; Bi, H.; Xu, F.; Huang, F. Nitrogen-Doped Mesoporous Carbon of Extraordinary Capacitance for Electrochemical Energy Storage. *Science* **2015**, *350*, 1508−1513.

(16) Jeong, H. M.; Lee, J. W.; Shin, W. H.; Choi, Y. J.; Shin, H. J.; Kang, J. K.; Choi, J. K. Nitrogen-Doped Graphene for High-Performance Ultracapacitors and the Importance of Nitrogen-Doped Sites at Basal Planes. *Nano Lett.* **2011**, *11*, 2472−2477.

(17) Pinkert, K.; Oschatz, M.; Borchardt, L.; Klose, M.; Zier, M.; Nickel, W.; Giebeler, L.; Oswald, S.; Kaskel, S.; Eckert, J. Role of Surface Functional Groups in Ordered Mesoporous Carbide-Derived Carbon/Ionic Liquid Electrolyte Double-Layer Capacitor Interfaces. *ACS Appl. Mater. Interfaces* **2014**, *6*, 2922−2928.

(18) Liu, Y.; Shen, Y.; Sun, L.; Li, J.; Liu, C.; Ren, W.; Li, F.; Gao, L.; Chen, J.; Liu, F.; Sun, Y.; Tang, N.; Cheng, H.-M.; Du, Y. Elemental Superdoping of Graphene and Carbon Nanotubes. *Nat. Commun.* **2016**, *7*, 10921.

(19) Lei, Z.; Zhang, J.; Zhang, L. L.; Kumar, N. A.; Zhao, X. S. Functionalization of Chemically Derived Graphene for Improving Its Electrocapacitive Energy Storage Properties. *Energy Environ. Sci.* **2016**, *9*, 1891−1930.

(20) Zhang, Z.; Wang, L.; Li, Y.; Wang, Y.; Zhang, J.; Guan, G.; Pan, Z.; Zheng, G.; Peng, H. Nitrogen-Doped Core-Sheath Carbon Nanotube Array for Highly Stretchable Supercapacitor. *Adv. Energy Mater.* **2017**, *7*, 1601814.

(21) Xu, Y.; Lin, Z.; Huang, X.; Wang, Y.; Huang, Y.; Duan, X. Functionalized Graphene Hydrogel-Based High-Performance Supercapacitors. *Adv. Mater.* **2013**, *25*, 5779−5784.

(22) Qie, L.; Chen, W.; Xu, H.; Xiong, X.; Jiang, Y.; Zou, F.; Hu, X.; Xin, Y.; Zhang, Z.; Huang, Y. Synthesis of Functionalized 3D Hierarchical Porous Carbon for High-Performance Supercapacitors. *Energy Environ. Sci.* **2013**, *6*, 2497−2504.

(23) Dyatkin, B.; Zhang, Y.; Mamontov, E.; Kolesnikov, A. I.; Cheng, Y.; Meyer, H. M., III; Cummings, P. T.; Gogotsi, Y. Influence of Surface Oxidation on Ion Dynamics and Capacitance in Porous and Nanoporous Carbon Electrodes. *J. Phys. Chem. C* **2016**, *120*, 8730−8741.

(24) Qu, J.; Geng, C.; Lv, S.; Shao, G.; Ma, S.; Wu, M. Nitrogen, Oxygen and Phosphorus Decorated Porous Carbons Derived from Shrimp Shells for Supercapacitors. *Electrochim. Acta* **2015**, *176*, 982−988.

(25) Huang, P.; Lethien, C.; Pinaud, S.; Brousse, K.; Laloo, R.; Turq, V.; Respaud, M.; Demortière, A.; Daffos, B.; Taberna, P. L.; Chaudret, B.; Gogotsi, Y.; Simon, P. On-Chip and Freestanding Elastic Carbon Films for Micro-Supercapacitors. *Science* **2016**, *351*, 691−695.

(26) Largeot, C.; Portet, C.; Chmiola, J.; Taberna, P.-L.; Gogotsi, Y.; Simon, P. Relation Between the Ion Size and Pore Size for an Electric Double-Layer Capacitor. *J. Am. Chem. Soc.* **2008**, *130*, 2730−2731.

(27) Chmiola, J.; Largeot, C.; Taberna, P.-L.; Simon, P.; Gogotsi, Y. Monolithic Carbide-Derived Carbon Films for Micro-Supercapacitors. *Science* **2010**, *328*, 480−483.

(28) Pech, D.; Brunet, M.; Durou, H.; Huang, P.; Mochalin, V.; Gogotsi, Y.; Taberna, P.-L.; Simon, P. Ultrahigh-Power Micrometre-Sized Supercapacitors Based on Onion-Like Carbon. *Nat. Nanotechnol.* **2010**, *5*, 651−654.

(29) Huang, P.; Heon, M.; Pech, D.; Brunet, M.; Taberna, P.-L.; Gogotsi, Y.; Lofland, S.; Hettinger, J. D.; Simon, P. Micro-Supercapacitors from Carbide Derived Carbon (CDC) Films on Silicon Chips. *J. Power Sources* **2013**, *225*, 240−244.

(30) Dash, R. K.; Nikitin, A.; Gogotsi, Y. Microporous Carbon Derived from Boron Carbide. *Microporous Mesoporous Mater.* **2004**, *72*, 203−208.

(31) Létiche, M.; Brousse, K.; Demortière, A.; Huang, P.; Daffos, B.; Pinaud, S.; Respaud, M.; Chaudret, B.; Roussel, P.; Buchaillot, L.; Taberna, P. L.; Simon, P.; Lethien, C. Sputtered Titanium Carbide Thick Film for High Areal Energy on Chip Carbon-Based Micro-Supercapacitors. *Adv. Funct. Mater.* **2017**, *27*, 1606813.

(32) Kim, M.; Oh, I.; Kim, J. Superior Electric Double Layer Capacitors Using Micro- and Mesoporous Silicon Carbide Sphere. *J. Mater. Chem. A* **2015**, *3*, 3944−3951.

(33) Gogotsi, Y.; Nikitin, A.; Ye, H.; Zhou, W.; Fischer, J. E.; Yi, B.; Foley, H. C.; Barsoum, M. W. Nanoporous Carbide-Derived Carbon with Tunable Pore Size. *Nat. Mater.* **2003**, *2*, 591−594.

(34) Zheng, J.; Ekström, T. C.; Gordeev, S. K.; Jacob, M. Carbon with an Onion-Like Structure Obtained by Chlorinating Titanium Carbide. *J. Mater. Chem.* **2000**, *10*, 1039−1041.

(35) Rose, M.; Korenblit, Y.; Kockrick, E.; Borchardt, L.; Oschatz, M.; Kaskel, S.; Yushin, G. Hierarchical Micro- and Mesoporous Carbide-Derived Carbon as a High-Performance Electrode Material in Supercapacitors. *Small* **2011**, *7*, 1108−1117.

(36) Liu, H.-J.; Wang, J.; Wang, C.-X.; Xia, Y.-Y. Ordered Hierarchical Mesoporous/Microporous Carbon Derived from Mesoporous Titanium-Carbide/Carbon Composites and Its Electrochemical Performance in Supercapacitor. *Adv. Energy Mater.* **2011**, *1*, 1101−1108.

(37) Presser, V.; Heon, M.; Gogotsi, Y. Carbide-Derived Carbons − from Porous Networks to Nanotubes and Graphene. *Adv. Funct. Mater.* **2011**, *21*, 810−833.

(38) Liu, D.; Jia, Z.; Wang, D. Preparation of Hierarchically Porous Carbon Nanosheet Composites with Graphene Conductive Scaffolds for Supercapacitors: An Electrostatic-Assistant Fabrication Strategy. *Carbon* **2016**, *100*, 664−677.

(39) Zhou, J.; Yuan, X.; Xing, W.; Si, W.; Zhuo, S. Capacitive Performance of Mesoporous Carbons Derived from the Citrates in Ionic Liquid. *Carbon* **2010**, *48*, 2765−2772.

(40) He, X.; Zhang, N.; Shao, X.; Wu, M.; Yu, M.; Qiu, J. A Layered-Template-Nanospace-Confinement Strategy for Production of Corrugated Graphene Nanosheets from Petroleum Pitch for Supercapacitors. *Chem. Eng. J.* **2016**, *297*, 121−127.

(41) Su, H.; Zhang, H.; Liu, F.; Chun, F.; Zhang, B.; Chu, X.; Huang, H.; Deng, W.; Gu, B.; Zhang, H.; Zheng, X.; Zhu, M.; Yang, W. High Power Supercapacitors Based on Hierarchically Porous Sheet-Like Nanocarbons with Ionic Liquid Electrolytes. *Chem. Eng. J.* **2017**, *322*, 73−81.

(42) Lee, C.-W.; Yoon, S.-B.; Kim, H.-K.; Youn, H.-C.; Han, J.; Roh, K. C.; Kim, K.-B. A Two-Dimensional Highly Ordered Mesoporous Carbon/Graphene Nanocomposite for Electrochemical Double Layer Capacitors: Effects of Electrical and Ionic Conduction Pathways. *J. Mater. Chem. A* **2015**, *3*, 2314−2322.

(43) Wu, M.; Ai, P.; Tan, M.; Jiang, B.; Li, Y.; Zheng, J.; Wu, W.; Li, Z.; Zhang, Q.; He, X. Synthesis of Starch-Derived Mesoporous Carbon for Electric Double Layer Capacitor. *Chem. Eng. J.* **2014**, *245*, 166−172.

(44) Tolosa, A.; Krüner, B.; Jäckel, N.; Aslan, M.; Vakifahmetoglu, C.; Presser, V. Electrospinning and Eletrospraying of Silicon Oxycarbide-Derived Nanoporous Carbon for Supercapacitor Electrodes. *J. Power Sources* **2016**, *313*, 178−188.

(45) Oschatz, M.; Pré, P.; Dörfler, S.; Nickel, W.; Beaunier, P.; Rouzaud, J.-N.; Fischer, C.; Brunner, E.; Kaskel, S. Nanostructure Characterization of Carbide-Derived Carbons by Morphological Analysis of Transmission Electron Microscopy Images Combined with Physisorption and Raman Spectroscopy. *Carbon* **2016**, *105*, 314−322.

(46) Kou, Z.; Guo, B.; Zhao, Y.; Huang, S.; Meng, T.; Zhang, J.; Li, W.; Amiinu, I. S.; Pu, Z.; Wang, M.; Jiang, M.; Liu, X.; Tang, Y.; Mu, S. Molybdenum Carbide-Derived Chlorine-Doped Ordered Mesoporous Carbon with Few-Layered Graphene Walls for Energy Storage Applications. *ACS Appl. Mater. Interfaces* **2017**, *9*, 3702−3712.

(47) Li, Z.; Song, B.; Wu, Z.; Lin, Z.; Yao, Y.; Moon, K.-S.; Wong, C. P. 3D Porous Graphene with Ultrahigh Surface Area for Microscale Capacitive Deionization. *Nano Energy* **2015**, *11*, 711−718.

(48) Li, Y.; Wang, G.; Wei, T.; Fan, Z.; Yan, P. Nitrogen and Sulfur Co-Doped Porous Carbon Nanosheets Derived from Willow Catkin for Supercapacitors. *Nano Energy* **2016**, *19*, 165−175.

(49) Zhang, S.; Ikoma, A.; Ueno, K.; Chen, Z.; Dokko, K.; Watanabe, M. Protic-Salt-Derived Nitrogen/Sulfur-Codoped Mesoporous Carbon for the Oxygen Reduction Reaction and Supercapacitors. *ChemSusChem* **2015**, *8*, 1608−1617.

(50) Zera, E.; Nickel, W.; Hao, G. P.; Vanzetti, L.; Kaskel, S.; Sorarù, G. D. Nitrogen Doped Carbide Derived Carbon Aerogels by Chlorine Etching of a SiCN Aerogel. *J. Mater. Chem. A* **2016**, *4*, 4525−4533.

(51) Zhang, D.; Zheng, L.; Ma, Y.; Lei, L.; Li, Q.; Li, Y.; Luo, H.; Feng, H.; Hao, Y. Synthesis of Nitrogen- and Sulfur-Codoped 3D Cubic-Ordered Mesoporous Carbon with Superior Performance in Supercapacitors. *ACS Appl. Mater. Interfaces* **2014**, *6*, 2657−2665.

(52) Gao, F.; Shao, G.; Qu, J.; Lv, S.; Li, Y.; Wu, M. Tailoring of Porous and Nitrogen-Rich Carbons Derived from Hydrochar for High-Performance Supercapacitor Electrodes. *Electrochim. Acta* **2015**, *155*, 201−208.

(53) Graupner, R.; Abraham, J.; Vencelová, A.; Seyller, T.; Hennrich, F.; Kappes, M. M.; Hirsch, A.; Ley, L. Doping of Single-Walled Carbon Nanotube Bundles by Brønsted Acids. *Phys. Chem. Chem. Phys.* **2003**, *5*, 5472−5476.

(54) Papirer, E.; Lacroix, R.; Donnet, J.-B.; Nansé, G.; Fioux, P. XPS Study of the Halogenation of Carbon Black − Part 2. Chlorination. *Carbon* **1995**, *33*, 63−72.

(55) Presser, V.; Zhang, L.; Niu, J. J.; McDonough, J.; Perez, C.; Fong, H.; Gogotsi, Y. Flexible Nano-Felts of Carbide-Derived Carbon with Ultra-High Power Handling Capability. *Adv. Energy Mater.* **2011**, *1*, 423−430.

(56) Zhao, Q.; Wang, X.; Liu, J.; Wang, H.; Zhang, Y.; Gao, J.; Liu, J.; Lu, Q. Surface Modification and Performance Enhancement of Carbon Derived from Chromium Carbide for Supercapacitor Applications. *J. Electrochem. Soc.* **2015**, *162*, A845−A851.

(57) Xu, J.; Wu, C.; Yan, P.; Wang, J.; Zhang, R.; Zhang, X.; Jin, J. Enhanced Electrochemical Performance of Graphitized Carbide-Derived Carbon in Alkaline Electrolyte. *Electrochim. Acta* **2015**, *174*, 411−416.

(58) Pérez, C. R.; Yeon, S.-H.; Ségalini, J.; Presser, V.; Taberna, P.-L.; Simon, P.; Gogotsi, Y. Structure and Electrochemical Performance of Carbide-Derived Carbon Nanopowders. *Adv. Funct. Mater.* **2013**, *23*, 1081−1089.

(59) Wu, C.; Gao, J.; Zhao, Q.; Zhang, Y.; Bai, Y.; Wang, X.; Wang, X. Preparation and Supercapacitive Behaviors of the Ordered Mesoporous/Microporous Chromium Carbide-Derived Carbons. *J. Power Sources* **2014**, *269*, 818−824.

(60) Yan, P.; Xu, J.; Wu, C.; Gu, Y.; Zhang, X.; Zhang, R.; Song, Y. High-Power Supercapacitors Based on Hierarchical Porous Nanometer-Sized Silicon Carbide-Derived Carbon. *Electrochim. Acta* **2016**, *189*, 16−21.

(61) Oschatz, M.; Zeiger, M.; Jäckel, N.; Strubel, P.; Borchardt, L.; Reinhold, R.; Nickel, W.; Eckert, J.; Presser, V.; Kaskel, S. Emulsion Soft Templating of Carbide-Derived Carbon Nanospheres with Controllable Porosity for Capacitive Electrochemical Energy Storage. *J. Mater. Chem. A* **2015**, *3*, 17983−17990.

(62) Ariyanto, T.; Laziz, A. M.; Gläsel, J.; Zhang, G.-R.; Garbes, J.; Etzold, B. J. M. Producing High Quality Carbide-Derived Carbon from Low Quality Byproducts Stemming from SiC Production. *Chem. Eng. J.* **2016**, *283*, 676−681.

(63) Yoo, H. D.; Jang, J. H.; Ryu, J. H.; Park, Y.; Oh, S. M. Impedance Analysis of Porous Carbon Electrodes to Predict Rate Capability of Electric Double-Layer Capacitors. *J. Power Sources* **2014**, *267*, 411−420.

(64) Prabaharan, S. R. S.; Vimala, R.; Zainal, Z. Nanostructured Mesoporous Carbon as Electrodes for Supercapacitors. *J. Power Sources* **2006**, *161*, 730−736.

(65) Dutta, S.; Bhaumik, A.; Wu, K. C.-W. Hierarchically Porous Carbon Derived from Polymers and Biomass: Effect of Interconnected Pores on Energy Applications. *Energy Environ. Sci.* **2014**, *7*, 3574−3592.

(66) Pan, L.; Wang, Y.; Hu, H.; Li, X.; Liu, J.; Guan, L.; Tian, W.; Wang, X.; Li, Y.; Wu, M. 3D Self-Assembly Synthesis of Hierarchical Porous Carbon from Petroleum Asphalt for Supercapacitors. *Carbon* **2018**, *134*, 345−353.

(67) Xie, X.; He, X.; Zhang, H.; Wei, F.; Xiao, N.; Qiu, J. Interconnected Sheet-Like Porous Carbons from Coal Tar by a Confined Soft-Template Strategy for Supercapacitors. *Chem. Eng. J.* **2018**, *350*, 49−56.

(68) Kim, M.; Oh, I.; Kim, J. Effects of Different Electrolytes on the Electrochemical and Dynamic Behavior of Electric Double Layer

Capacitors Based on a Porous Silicon Carbide Electrode. *Phys. Chem. Chem. Phys.* **2015**, *17*, 16367−16374.

(69) Xu, B.; Wang, H.; Zhu, Q.; Sun, N.; Anasori, B.; Hu, L.; Wang, F.; Guan, Y.; Gogotsi, Y. Reduced Graphene Oxide as a Multi-Functional Conductive Binder for Supercapacitor Electrodes. *Energy Storage Mater.* **2018**, *12*, 128−136.